Dynamic Potential Sputtering of Lunar Analogue Material by Solar Wind Ions

Paul S. Szabo[1,*], Herbert Biber[1], Noah Jäggi[2], Matthias Brenner[1], David Weichselbaum[1], Anna Niggas[1], Reinhard Stadlmayr[1], Daniel Primetzhofer[3], Andreas Nenning[4], Andreas Mutzke[5], Markus Sauer[6], Jürgen Fleig[4], Annette Foelske-Schmitz[6], Klaus Mezger[7], Helmut Lammer[8], André Galli[2], Peter Wurz[2], and Friedrich Aumayr[1,*]

[1] *Institute of Applied Physics, TU Wien, Wiedner Hauptstraße 8-10, 1040 Vienna, Austria*

[2] *Physics Institute, University of Bern, Sidlerstrasse 5, 3012 Bern, Switzerland*

[3] *Department of Physics and Astronomy, Uppsala University, Ångströmlaboratoriet, Lägerhyddsvägen 1, 752 37 Uppsala, Sweden*

[4] *Institute of Chemical Technologies and Analytics, TU Wien, Getreidemarkt 9, 1060 Vienna, Austria*

[5] *Max-Planck-Institut für Plasmaphysik, Wendelsteinstraße 1, 17491 Greifswald, Germany*

[6] *Analytical Instrumentation Center, TU Wien, Getreidemarkt 9, 1060 Vienna, Austria*

[7] *Institute of Geological Sciences, University of Bern, Baltzerstraße 1+3, 3012 Bern, Switzerland*

[8] *Space Research Institute (IWF), Austrian Academy of Sciences, Schmiedlstr. 6, 8042 Graz, Austria*

[*]Corresponding authors : szabo@iap.tuwien.ac.at, aumayr@iap.tuwien.ac.at

ABSTRACT

Pyroxenes ($(Ca,Mg,Fe,Mn)_2Si_2O_6$) belong to the most abundant rock forming minerals that make up the surface of rocky planets and moons. Therefore sputtering of pyroxenes by solar wind ions has to be considered as a very important process for modifying the surface of planetary bodies. This is increased due to potential sputtering by multiply charged ions and to quantify this effect, sputtering of wollastonite ($CaSiO_3$) by He^{2+} ions was investigated. Thin films of $CaSiO_3$ deposited on a quartz crystal microbalance were irradiated allowing precise in-situ real time sputtering yield measurements. Experimental results were compared with SDTrimSP simulations, which were improved by adapting the used input parameters. On freshly prepared surfaces He^{2+} ions show a significant increase in sputtering compared to equally fast He^{+} ions. However, the yield decreases exponentially with fluence, reaching a lower steady state after sputtering of the first few monolayers. Experiments using Ar^{8+} ions show a similar behavior, which is qualitatively explained by a preferential depletion of surface oxygen due to potential sputtering. A corresponding quantitative model is applied and the observed potential sputtering behaviors of both He and Ar are reproduced very well. The results of these calculations support the assumption that mainly O atoms are affected by potential sputtering. Based on our findings, we discuss the importance of potential sputtering for the solar wind eroding the lunar surface. Estimated concentration changes and sputtering yields are both in line with previous modeling for other materials, allowing a consistent view on the effects of solar wind potential sputtering.

KEYWORDS

Solar wind (1534), Exosphere (499), The Moon (1692), Mercury (planet) (1024), Laboratory astrophysics (2004), Lunar composition (948)

1. INTRODUCTION

Ion-induced sputtering as part of space weathering is a key aspect to the erosion of surfaces of planetary bodies due to solar wind ions that has to be investigated in detail (Hapke 2001). Laboratory sputtering experiments with mineral analogue samples are rare and therefore most models of space weathering and exosphere creation estimate sputtering yields or rely on numerically calculated values (see for example (Kallio & Janhunen 2003; Killen et al. 2007; Pfleger et al. 2015; Wurz et al. 2018; Wurz et al. 2007)). Numerical simulations are mostly performed with codes based on the binary collision approximation (BCA). In planetary sciences this is often done with TRIM simulations included in the SRIM package (Ziegler, Ziegler, & Biersack 2010). Especially for plasma-wall interaction in nuclear fusion reactors, dynamic 3D-BCA programs such as SDTrimSP (Mutzke et al. 2019) or TRI3DYN (Möller 2014) are more established (for examples of such applications see (Oberkofler et al. 2015; Stadlmayr et al. 2018; Stadlmayr et al. 2019) or (Arredondo et al. 2019)). These programs are well-suited for simulating kinetic sputtering due to the ion-induced collision cascade.

However, some effects are not included in these simulations, such as the sputtering of insulating targets by the potential energy of multiply charged ions, termed "potential sputtering" (Aumayr & Winter 2004). During space weathering, potential sputtering is an additional contribution to the sputtering by He^{2+} and heavier multiply charged ions in the solar wind. Some investigations exist for the potential sputtering effects of the solar wind. Both experiments and/or calculations have been done for the lunar simulants 'KREEP' (Barghouty et al. 2011) and 'JSC-1A' (Alnussirat et al. 2018; Meyer et al. 2011) as well as for thin films deposited from anorthite (Hijazi et al. 2017; Hijazi et al. 2014). However, in general the understanding of potential sputtering contributions to space weathering is still lacking and more experiments with relevant analogue minerals are needed.

To further investigate solar wind sputtering, we have performed corresponding irradiations on thin films deposited from wollastonite ($CaSiO_3$). Here the pyroxenoid wollastonite has been used as an analogue for the lunar surface. It can also be seen as an analogue to the general pyroxene contributions to bodies such as the Moon or Mercury, where pyroxene minerals (together with plagioclase) make up a significant amount of the respective surfaces (Cremonese et al. 2005; Yamashita et al. 2012).

First results from these experiments were presented in a previous publication (Szabo et al. 2018). Kinetic sputtering for H^+ and Ar^+ was found to be in good agreement with SDTrimSP, which gives better results for Ar, and SRIM, which is better for H. Furthermore, considerable potential sputtering contributions were observed for higher Ar charge states. Although Ar is only a minor constituent of the solar wind, it is a suitable analogue for the heavy ion contribution in the solar wind allowing to get more insight of the fundamental physics of potential sputtering of minerals. A dependence of the potential sputtering yield on the ions' potential energy similar to Hijazi et al. was found (Hijazi, et al. 2017).

Significant deviations from the kinetic sputtering yield already occur for Ar^{2+} ions, which carry a potential energy of 41 eV (DREEBIT 2018). As a first assumption, potential sputtering was taken to be independent of the ion species (Szabo, et al. 2018), with only the potential energy being important. Therefore, He^{2+} should cause an even higher potential sputtering since these ions carry a potential energy of 77 eV (DREEBIT 2018). He^{2+} is much more prominent in the solar wind than heavier ions (Wurz 2005) and will probably play the most important role for potential sputtering. Previously we have used data from Ar^{q+} measurements to estimate the potential sputtering for He^{2+} ions. We predicted them to be about five times higher than the kinetic sputtering yield at the He solar wind energy of 4 keV (see Figure 1) (Szabo, et al. 2018). This would make He^{2+} the most significant source of solar wind sputtering. We have now performed experiments with singly and doubly charged He ions. Measurements presented in this manuscript aim to determine He^{2+} sputtering yields and to clarify our previous extrapolation.

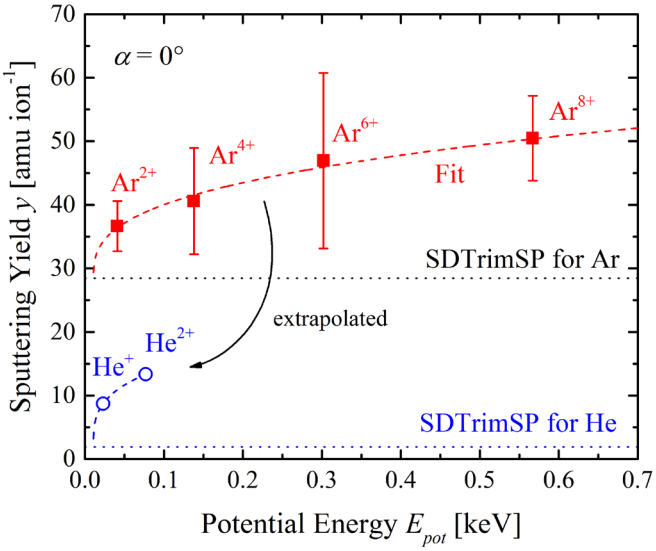

Figure 1: Previously published measured sputtering yields for impact of 8 keV Ar^{q+} ($2 \leq q \leq 8$) ions on $CaSiO_3$ under normal incidence as a function of the ions' potential energy (red data points, see (Szabo, et al. 2018)). Results from SDTrimSP were used to estimate the yield of kinetic sputtering (black dotted line). The potential sputtering contribution (difference between measured yields and results from SDTrimSP) can be fitted by the formula $\alpha\ (E_{pot} - 2E_B)^{\beta}$ (red dashed line) with twice the material's band gap as a threshold energy (Szabo, et al. 2018). This fit was used to extrapolate the expected potential sputtering yield for 4 keV He^{+} and He^{2+} (open blue symbols, kinetic contribution again taken from SDTrimSP).

2. METHODS

2.1 Experimental Setup

All presented sputtering experiments were performed with the same ion beam setup as described earlier (Szabo, et al. 2018). Sputtering yields are measured with the Quartz Crystal Microbalance (QCM) technique (Hayderer et al. 1999a), which allows in-situ observation of thin film mass changes in real time by recording the resonance frequency of the quartz's thickness oscillation. Samples are mounted on a rotatable sample holder allowing measurements under different angles of incidence. Experiments at different temperatures are possible by heating the sample, however, all presented experiments were done at room temperature.

He irradiations were performed using both 4 keV ^4He and 3 keV ^3He at solar wind velocities of 1 keV amu^{-1}. ^3He had to be used to guarantee a clean He^{2+} ion beam that was not contaminated with molecular H_2^+ ions. Due to the big difference in sputtering yields by H and He (about one order of magnitude), already small but unavoidable hydrogen contaminations of the ion source would lead to errors in the measurement. Using ^3He gas allows distinguishing $^3He^{2+}$ (m/q = 3/2) from any H contaminations (m/q = 2 for H_2^+) in the magnetic sector field for mass-over-charge separation. A small hydrogen component of the Electron Cyclotron Resonance (ECR) ion source plasma has to be expected due to a source base pressure of 10^{-7} mbar. From acquired spectra during ^3He measurements a H particle flux component of up to 30% can occur if they are not separated. This would lead to a significant underestimation of measured He^{2+} sputtering yields.

2.2 Sample Preparation and Analysis

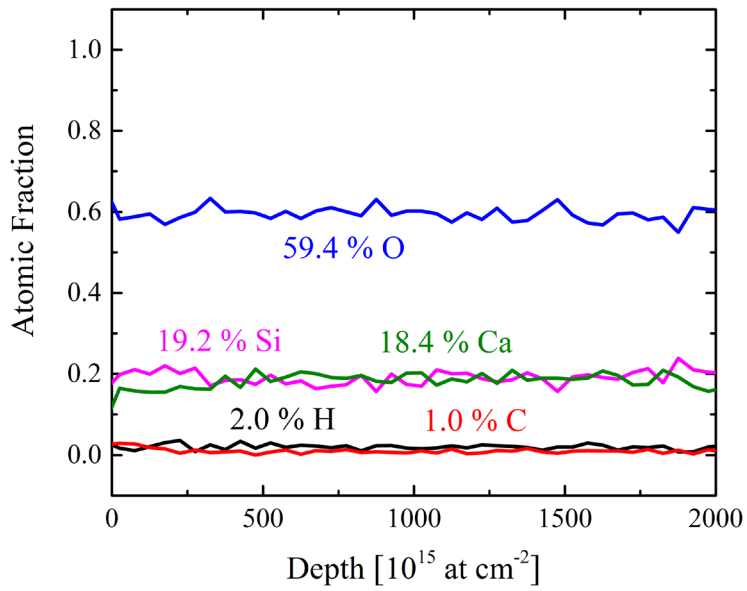

Figure 2: ToF-ERDA analysis of a 700 nm $CaSiO_3$ film for the first 2000×10^{15} at cm^{-2} (roughly 260 nm), where this method can reliably probe the elemental composition of the sample. The analysis shows that the concentrations of Ca (green), Si (pink) and O (blue) are close to $CaSiO_3$. Only minor contaminations of H (black) and C (red) are observed.

Similar to the previous experiments (Szabo, et al. 2018), thin amorphous $CaSiO_3$ films deposited on our quartz crystals by Pulsed Laser Deposition (PLD) were used for the sputter yield measurements. The PLD was performed in 0.04 mbar O_2 atmosphere at a substrate temperature of ~270 °C with the laser operating at 5 Hz and a fluence of 2 J cm^{-2} $pulse^{-1}$ on the sample for 60 minutes.

The films were analyzed with Rutherford Backscattering Spectrometry (RBS) and Time-of-Flight Elastic Recoil Detection Analysis (ToF-ERDA), from which sample thickness and depth dependent elemental concentrations could be obtained. RBS using a 2 MeV He beam showed that the sample thicknesses of the films varied between 250×10^{15} at cm^{-2} and 5300×10^{15} at cm^{-2} depending on the PLD parameters (varying number of laser pulses). Assuming a $CaSiO_3$ bulk density of 2.86 g cm^{-3} (Deer, Howie, & Zussman 1997), this corresponds to an actual film thickness between about 30 and 700 nm. ToF-ERDA analysis with 36 MeV iodine ions proves that the PLD films are very similar to the stoichiometric $CaSiO_3$ composition. Figure 2 shows the ERDA analysis of the 700 nm film as an example. Close to the surface, slightly less Ca than Si is observed, which is consistent with the sputter-XPS results for samples of the same batch (Szabo, et al. 2018). However, across the whole analyzed area the average composition is 18.4 % Ca, 19.2 % Si, 59.4 % O and only 2.0 % H and 1.0 % C. Similar results were also found for the 30 nm film (18.3 % Ca, 20.0 % Si, 59.5 % O, 1.2 % H and 1.0 % C), showing that PLD provides good sample compositions also at low film thicknesses. Therefore, we conclude that the film composition is close to stoichiometric $CaSiO_3$ across the whole film.

XPS analysis was also done for samples that were used for the present investigations. Similar to previous results (Szabo, et al. 2018) O and C contents are higher than reported from ToF-ERDA. As surface contamination effects cannot be completely excluded to influence XPS results, the ToF-ERDA analysis was taken as a reference of the film's composition being very close to $CaSiO_3$.

2.3 Kinetic Sputtering Simulations

Kinetic sputtering yields were simulated with the BCA programs SDTrimSP and SRIM. In previous investigations, it was found that SDTrimSP can reproduce the angular dependence of Ar sputtering yields when taking into account the sample composition from XPS (Szabo, et al. 2018). There we also stated that

the nominal $CaSiO_3$ composition leads to a significant overestimation of sputtering yields. However, the ToF-ERDA results in Figure 2 indicate that small deviations from the stoichiometric composition are only present at the surface. For prolonged sputtering experiments, they should not play a significant role and an agreement with a simulation using the stoichiometric $CaSiO_3$ composition should also be found.

For BCA simulations, especially the surface binding energies of the target elements play an important role. According to Sigmund's sputtering theory, the sputtering yield is inversely proportional to the surface binding energy (Sigmund 1969). In general, the heat of sublimation can be used as a good approximation for mono-elemental samples (Behrisch & Eckstein 2007), which are included as tabulated values in SRIM or SDTrimSP. However, for composite samples the surface binding energy usually represents an unknown quantity. Different theories have been developed to calculate these energies by using, for example, bond energies and electronegativity (Malherbe, Hofmann, & Sanz 1986), nearest-neighbor bond strengths (Kelly 1980) or the formation enthalpy (Möller & Posselt 2001). However, no universally accepted formalism for calculating unknown surface binding energies exists.

Together with using the $CaSiO_3$ bulk density of 2.86 g cm^{-3} (Deer, et al. 1997), we therefore adapted the surface binding energies to the results of 2 keV Ar^+ measurements for simulating the sputtering of $CaSiO_3$. This consistently leads to good agreement with experimental results for other energies as well. The choice of input parameters is described and justified in detail in the Appendix.

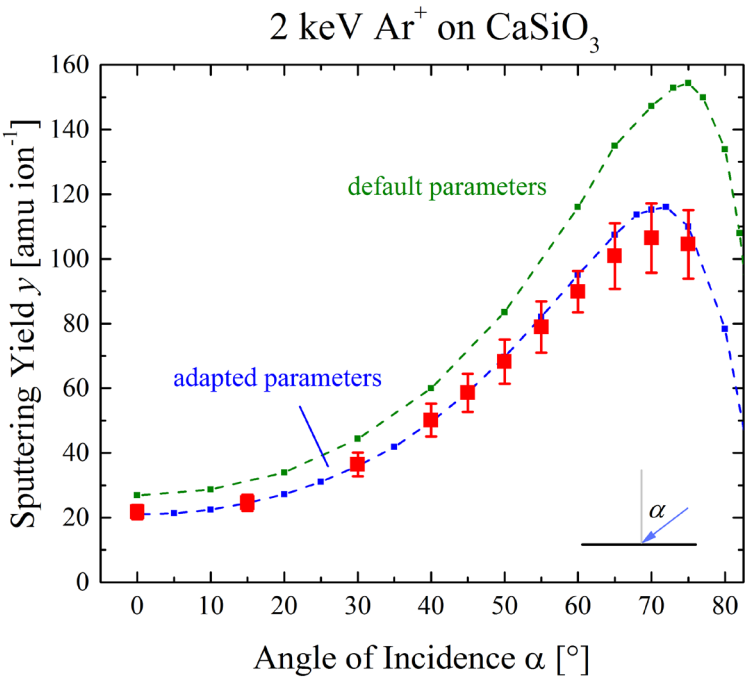

Figure 3: Comparison of different SDTrimSP simulations with experimental results (red) for 2 keV Ar^+ sputtering yields. Default parameters (green) overestimate the measured yields, while the adapted parameters (blue) give a better agreement.

The results of simulating kinetic sputtering by 2 keV Ar ions are shown in Figure 3. The experimental values (red, taken from (Szabo, et al. 2018)) are compared to a simulation using default parameters for SDTrimSP (green), leading to an overestimation of the experimental results. The adapted input parameters (see the Appendix) show improved agreement with the experiment (blue).

The plotted simulations were performed in the static mode of SDTrimSP. Dynamic simulations were done for selected angles using the adapted parameters, but there were only concentration changes of a few percent observed as well as no significant changes in the mass sputtering yield. These results are in line with experimental observations, where no substantial fluence dependence of the sputtering yield could be observed for the investigated fluences in the order of 10^{19} ions m^{-2}.

Steady state elemental sputtering yields correspond to the bulk elemental concentrations. With a well-known sample composition and good agreement with total mass sputtering yields, SDTrimSP should thus give a good quantification of the element sputtering yields. The adapted parameters are

therefore also used for the simulations of the kinetic sputtering contribution of He ions in the following sections.

3. SPUTTERING MEASUREMENTS

3.1 He^+ Sputtering

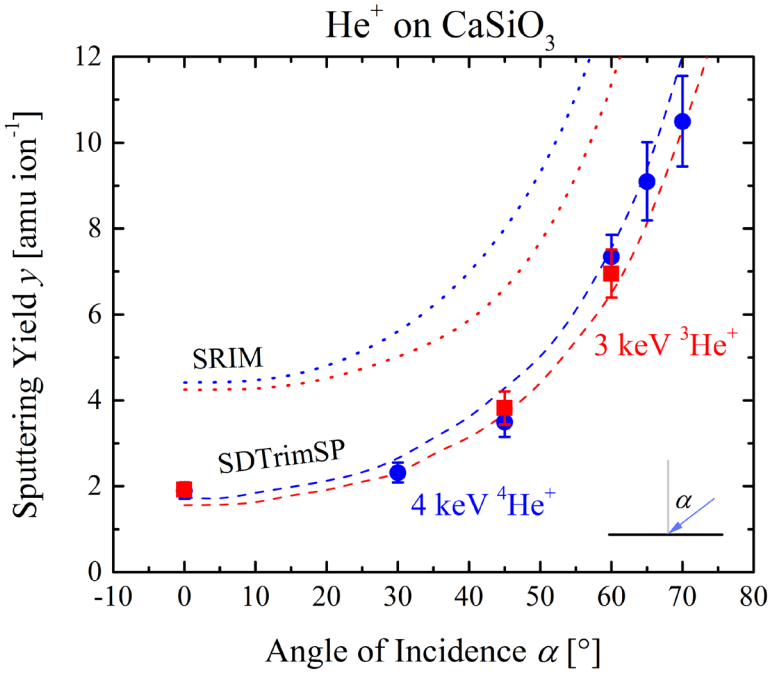

Figure 4: Comparison of the sputtering yields for 3 keV $^3He^+$ (red) and 4 keV $^4He^+$ (blue) bombardment. Experimental results are plotted for different angles of incidence together with simulation results from SDTrimSP (dashed lines) and SRIM (dotted lines).

First, sputtering with He^+ at approximate solar wind velocity (1 keV amu^{-1}) was investigated for 4 keV $^4He^+$ and for 3 keV $^3He^+$. ^4He is much more abundant than ^3He in the solar wind, but using ^3He was necessary for investigations with doubly charged He, as discussed in Section 2.1.

Figure 4 shows the measured sputtering yields for $^3He^+$ (red squares) and $^4He^+$ (blue circles) under different angles of incidence (taken with respect to the surface normal). For all investigated angles, the measured sputtering yields for both He isotopes at the same impact velocity coincide within their uncertainty limits. The experimental results are plotted

together with simulation results from SDTrimSP (dashed lines) and SRIM (dotted lines). Taking SRIM with default parameters as a reference for kinetic sputtering yields would significantly overestimate experimental sputtering yields. SDTrimSP, on the other hand, predicts sputtering yields mostly within the experimental error bars using our adapted simulation parameters (see Section 2.3 and the Appendix) in accordance with our findings for sputtering by Ar ions. Besides the absolute values, the simulation predicts the sputtering yields for the two He isotopes to be very similar at the same velocity, which agrees with experimental findings. As the ionization energies and therefore the potential energies are equal for both He isotopes, sputtering yields obtained with 3 keV ^{3}He can be used to describe solar wind sputtering with ^{4}He.

At the beginning of He irradiations on fresh samples, small net mass increases (up to Δm = 0.3 amu ion^{-1}) were observed due to projectile implantation. Only after fluences of about 1×10^{17} ions cm^{-2} for the case of normal incidence, a steady mass decrease corresponding to a constant sputtering yield could be found. On fresh samples, a combination of sputtering and implantation is expected, which makes the exact determination of sputtering yields difficult. After a certain fluence, the sample, however, will be He saturated within the implantation range. Then there will be an equilibrium between implanted He and resputtered He atoms (Hayderer, et al. 1999a). In this steady state, the only net mass increase is caused by sputtered wollastonite atoms and no correction for He implantation is necessary.

The experimental He^{+} sputtering yields presented in this paper were obtained after steady state was reached. Assuming constant sputtering during these irradiations until steady state, the observed implantation varied significantly. Over a predicted implantation depth of about 30 nm, the measured mass changes correspond to an implanted He concentration between 1% and 6%. For these concentrations, dynamic SDTrimSP simulations predict maximal sputtering yield reductions of 7% in the steady state compared to a simulation without He implantation. This value is close to the experimental uncertainties of the measured sputtering yields. Furthermore, dynamic SDTrimSP simulations in general do not show any significant sputtering yield changes due to preferential sputtering by prolonged He irradiation. Therefore, we conclude that the measured steady state yields are representative of He sputtering of $CaSiO_3$ regardless of any He implantation. Nevertheless, the exact interplay between He implantation and diffusion inside the sample causing the observed transient effect of the mass change is not yet fully understood.

3.2 He^{2+} Sputtering

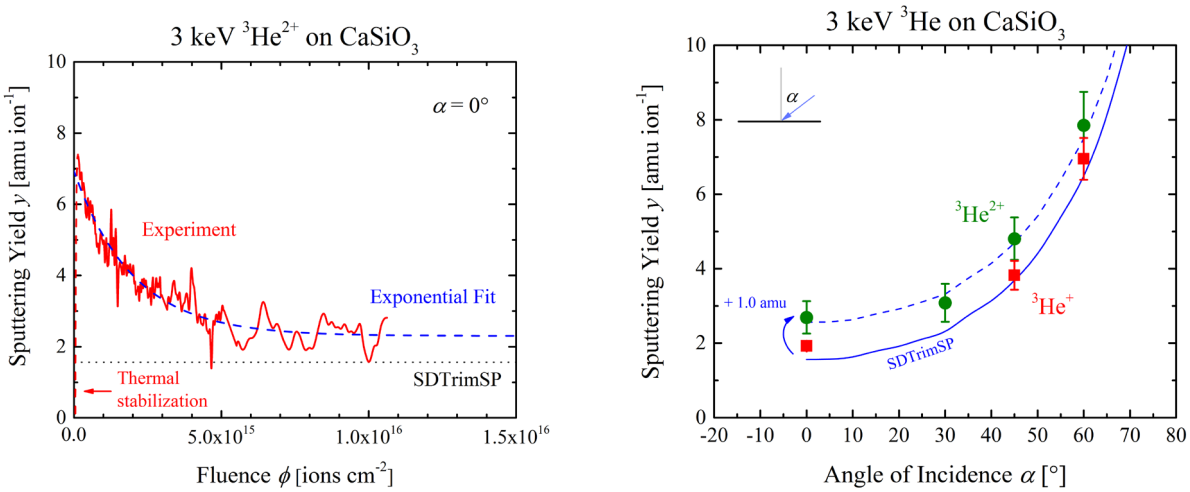

Figure 5: Left: Fluence dependence of the sputtering yield with continuous $^3He^{2+}$ bombardment at normal incidence. Measured yields (red) can be fitted with an exponential formula $y(\phi) = A \times exp(-\phi/\phi_0) + y_0$ (blue). The steady state sputtering yield is higher than the SDTrimSP simulation of the kinetic yield (black dotted line). The start of the measurement is influenced by thermal stabilization effects (red dashed line). Right: Angular dependence of the ^3He sputtering yields in the steady state. Experimental results of $^3He^+$ (red) and $^3He^{2+}$ (green) are compared to SDTrimSP simulations (blue full line). For all angles of incidence an offset to SDTrimSP of 1.0 amu is observed (blue dashed line).

Sputtering yields with $^3He^{2+}$ were measured for angles of incidence between 0° and 60° to investigate the influence of potential sputtering. To separate He^{2+} sputtering from implantation effects, the He^+ steady state under 0 degrees was taken as a starting point (after a previously applied fluence of about 10^{17} $^3He^+$ cm^{-2} as described in the previous sub-section) because no more He implantation should occur there.

As it is shown in the left image in Figure 5, detailed measurements of the sputtering yield at the beginning of the irradiation show a significantly increased sputter yield of about 7 amu ion^{-1} under normal incidence. It has to be noted that recording of the sputtering yield was only possible after

an already applied fluence of about 10^{14} ions cm^{-2}. Local heating of the quartz as a result of starting ion bombardment causes an additional frequency drift for a few minutes at the beginning of each measurement (red dashed line in the left image of Figure 5). During the irradiation, the sputter yield decreases until a steady state is reached after a fluence of 10^{16} ions cm^{-2} at a value much closer to the kinetic sputtering yield. The change of the sputtering yield y over fluence ϕ can be fitted with the formula $y(\phi) = A \times exp(-\phi/\phi_0) + y_0$ (blue dashed curve in the left image of Figure 5), which describes an exponential decay plus an offset y_0. For the measurement shown in Figure 5 the derived fit parameters are (A = 4.64 amu ion^{-1}, $\phi_0 = 1.998\times10^{15}$ ions cm^{-2}, $y_0 = 2.30$ amu ion^{-1}). The significant decrease of the sputtering yield indicates a change of the surface composition as a result of potential sputtering. However, the small fluence until steady state suggests that composition changes are confined to a thin region close to the surface. From the total frequency change until the steady state fluence (the value of 1.0×10^{16} ions cm^{-2} was chosen being five times the decay length ϕ_0 of the exponential fit), a total mass decrease of about 32×10^{15} amu cm^{-2} can be calculated. For this calculation, sputtering yields were assumed to be constant for the short fluence that is affected by thermal stabilization. The $CaSiO_3$ bulk density of 2.86 g cm^{-3} corresponds to an atomic density of 172×10^{15} amu cm^{-2} nm^{-1} and therefore, steady state is reached within the sputtering of the first few monolayers when no further He implantation is assumed. The right image in Figure 5 shows a compilation of steady state sputtering yields at different angles of incidence compared to the $^3He^+$ measurements from Figure 4. For the steady state yields of $^3He^{2+}$ a constant difference of about 1 amu ion^{-1} to the SDTrimSP prediction is observed for all investigated angles of incidence.

Similar fluence dependencies of potential sputtering were found in previous investigations of potential sputtering using SiO_2 (Varga et al. 1997), Al_2O_3 (Hayderer et al. 2001a) and MgO_x (Hayderer et al. 2001b) samples. In these studies the decrease of the sputtering yield was attributed to multiply charged ions causing a preferential sputtering of oxygen. Following the defect-mediated theory of potential sputtering, only O anions would desorb as a result of potential sputtering of an oxide target (Sporn et al. 1997). In this theory, an approaching ion that captures an electron from the insulating targets creates a localized electronic defect, a so-called self-trapped hole and self-trapped exciton, which subsequently leads to the desorption of neutral atoms (Hayderer et al. 1999b). Defect-mediated sputtering has been extensively investigated for alkali-halides showing precise agreement with the theory (Aumayr & Winter 2004; Hayderer, et al.

1999b; Neidhart et al. 1995a; Wirtz et al. 2000). For other materials where no formation of localized defects has been reported, no potential sputtering was observed (Aumayr & Winter 2004). In the case of an oxide sample, the self-trapped hole only affects the O anions and for electron irradiation of SiO_2 only O anion desorption is reported (Sporn, et al. 1997). Preferential O depletion by potential sputtering would then similarly cause a decrease in the surface O concentration for $CaSiO_3$ and therefore also a decrease of potential sputtering until a steady state is reached.

In the present work, identical initial conditions with a high potential sputtering yield could be reproduced in two ways: Either by sputter cleaning the sample's surface with Ar^+ ions or by oxygen flooding of the sample chamber (partial pressure of 10^{-3} – 10^{-4} mbar for several hours, both at room temperature or heated to 200°C). The first method corresponds to sputter removal of the O-depleted layers, thus exposing a stoichiometric $CaSiO_3$ surface again, while the oxygen flooding re-oxidizes a depleted surface. The success of both methods is a strong indication that the qualitative explanation proposed by Sporn, et al. (1997) as well as Hayderer, et al. (2001a) and Hayderer, et al. (2001b) is indeed correct.

3.3 Ar Sputtering

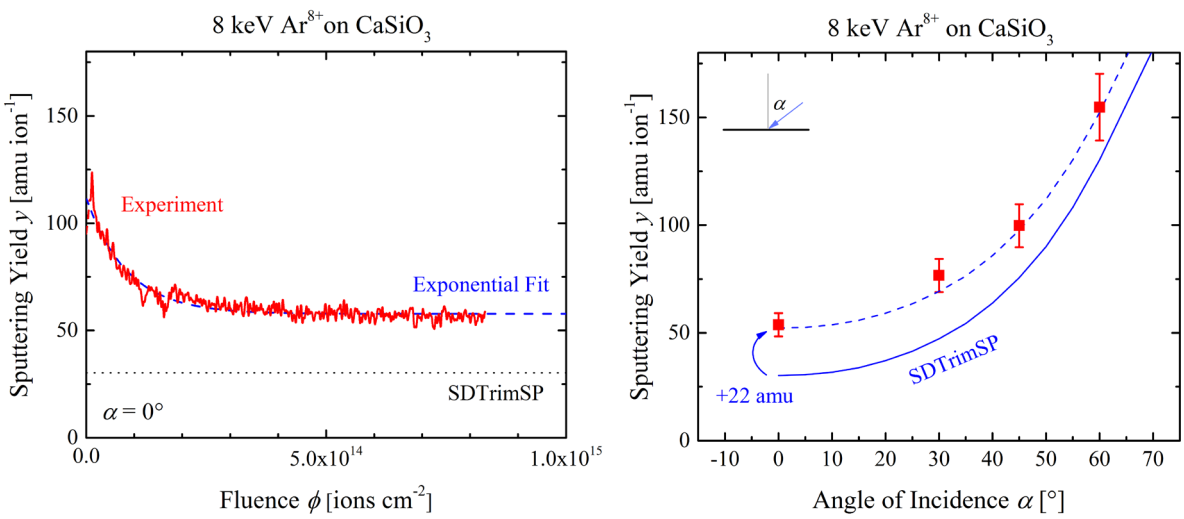

Figure 6: Left: Fluence dependence of the sputtering yield under continuous Ar^{8+} irradiation, which can again fitted with an exponential decrease. Fluences up to about 8×10^{12} ions cm^{-2} are affected by thermal stabilization

drifts as described in Section 3.2 (red dashed line). Right: Steady state sputtering yields of Ar^{8+} (red), which show a constant increase of 22 amu ion^{-1} compared to the SDTrimSP simulation for 8 keV Ar (blue dashed line and blue full line).

Fluence dependent sputtering yields were similarly found for Ar^{8+} measurements in a new, more detailed investigation presented in Figure 6. Contrary to He, no changing sputtering yields for prolonged Ar^{+} irradiation were observed, which indicates that Ar implantation is no significant effect for $CaSiO_3$. This was also assumed for measurements with Ar^{q+} with (q > 1), so no correction of the sputtering yield due to implantation effects had to be applied.

The measurements in Figure 6 show the same exponential decrease of the form $y(\phi) = A \times exp(-\phi/\phi_0) + y_0$ as described in the previous sub-section. The fit parameters for the measurement in the left image of Figure 6 are (A = 54.06 amu ion^{-1}, ϕ_0 = 8.52×10^{13} ions cm^{-2}, y_0 = 57.76 amu ion^{-1}). Fluences needed for steady state sputtering are therefore lower by about one order of magnitude compared to ^3He. Constant increases compared to the kinetic sputtering yields are found for all angles, in this case 22 amu ion^{-1} (see the right image in Figure 6). The mass decrease up until a fluence of 4.3×10^{14} ions cm^{-2} (five times the decay length of the exponential fit) is 29×10^{15} amu cm^{-2}, which is very similar to the observed value for ^3He irradiations. It is therefore a common scenario for both ^3He and Ar that steady state is reached after sputtering the first few atomic monolayers. The similar exponential decrease would also support the assumption of O depletion and therefore smaller potential sputtering effects.

Changing O sputtering yields were investigated by Meyer, et al. (2011) for Ar sputtering of lunar regolith simulant using a quadrupole mass spectrometer approach (QMS). In this study no significant changes were observed, but with their reported high beam fluxes of 10^{14} – 10^{15} ions cm^{-2} s^{-1}, it might be difficult to observe the pre-steady-state phase. Hijazi, et al. (2014) support constant sputtering yields with a remark about their anorthite measurements with Ar^{9+}, but they emphasize that further investigation is needed, especially due to unknown surface roughness effects. However, their later published calculations do include decreasing sputtering yields over fluence (Hijazi, et al. 2017). Even if potential sputtering only affects O atoms, a complete depletion of surface O would not be expected because kinetic sputtering will erode Ca and Si atoms and thus expose fresh O at the receding surface. Therefore, a lower than

initial but non-zero surface O concentration should be present in the equilibrium and the observed constant O sputter yields by Meyer, et al. (2011) could be in agreement with this explanation.

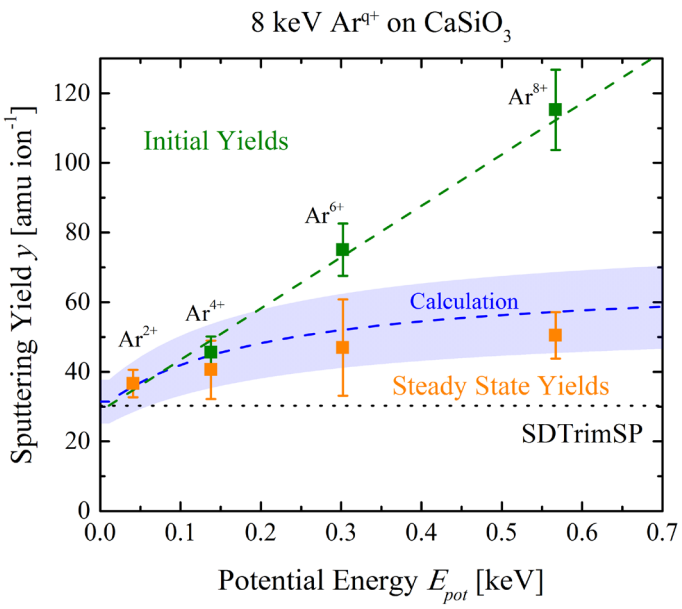

Figure 7: Ar sputtering yields for different potential energies of the ions, measured for the charge states 2+, 4+, 6+ and 8+. Sputtering yields at the beginning of the irradiation show a linear dependence (green) with E_{pot}. Steady state sputter yields depend much less on E_{pot} (orange). The calculation for dynamic potential sputtering is able to reproduce the measured steady state yields very well (blue dashed line, shaded area represents an uncertainty estimate, see Section 4).

Using both of the described in-situ sample preparation methods, initial sputtering yields (i.e. sputter yields at the beginning of the irradiation) were measured, and the results are shown in Figure 7. Measurements with 8 keV Ar^+ are not possible in the used setup due to a limited maximum acceleration voltage of 6 kV. Therefore, an SDTrimSP simulation is used as a reference for kinetic sputtering by 8 keV Ar ions, which is included as the black dotted line in Figure 7. The difference between this value and the measured sputtering yield is attributed to potential sputtering. For Ar charge states up to 8+ the potential sputtering yield is then proportional to the ion's potential energy (see the dashed green line in Figure 7). Its slope $\gamma_{Ar} \approx 9.2 \pm 1.8$ O atoms keV^{-1} or 147.4 ± 29.5 amu keV^{-1} gives the

dependence of the potential sputtering yield on the ion's potential energy, which will later be used to calculate potential sputtering effects numerically (see Section 4, Equation (4)). Sporn, et al. (1997) investigated this dependence for potential sputtering of SiO_2 using multiply charged Ar and Xe ions. There they found that the sputtering yields increase with 1 SiO_2 per 500 eV potential energy. This corresponds to 120 amu/keV and is therefore close to our findings for Ar^{q+} on $CaSiO_3$.

However, the initial sputtering yield of $^3He^{2+}$ that is shown in Figure 5 does not fit the same dependence. To describe the initial value of ~ 7 amu ion^{-1}, a different slope $\gamma_{He} \approx 5.1 \pm 1.3$ O atoms keV^{-1} (81.3 ± 20.0 amu keV^{-1}) has to be used. This would differ from our original assumption of a uniform potential sputtering behavior independent of ion species. Hijazi, et al. (2017) report such a close to linear uniform scaling for potential sputtering on anorthite, but find a lower slope of 3.2 O atoms keV^{-1}. This indicates a significant material dependence, which should be investigated in the future.

Figure 7 also shows the measured yields from Szabo, et al. (2018) in red. As they were measured multiple times to achieve better statistics, but without any oxidization or sputter cleaning in between, they have to be interpreted as steady state sputtering yields. These steady state yields were re-investigated for the present publication and agree with the previously published values.

4. DYNAMIC SPUTTERING MODEL

4.1 Theoretical Model

The previously shown measurements open up several questions that have yet to be answered quantitatively. It is necessary to investigate whether preferential sputtering of oxygen can explain the fluence dependence of potential sputtering. Furthermore, different steady state behaviors between He and Ar could also be explained in connection to this process due to the different kinetic sputtering yields. While potential sputtering presumably only erodes O atoms from $CaSiO_3$, a higher kinetic sputtering also causes additional removal of Ca and Si. This would bring more O to the surface leading to higher potential sputtering yields in the steady state.

To investigate if this qualitative assumption reproduces the previously shown measurements, a model for the dynamic sputtering consisting of a system of coupled differential equations was applied. A similar model has been used by Barghouty, et al. (2011), Hijazi, et al. (2017) and Alnussirat, et al. (2018) to extrapolate changes of surface compositions of lunar soil simulants and anorthite mineral due to solar wind sputtering from measured sputtering yields.

In the scope of this model, potential sputtering only causes the removal of O atoms. Cluster sputtering has been observed for slow highly charged ions (Schenkel et al. 1998), where a potential energy of over 100 keV is transferred to the sample. However, for solar wind-relevant sputtering the potential energies are much lower. For these potential energies in Ar^{q+} ($q \leq 9$) sputtering of LiF, cluster yields were found to be at least two orders of magnitudes below atomic sputtering yields (Neidhart et al. 1995b). This supports the assumption of only O atoms being eroded, especially for the important case of He^{2+} with a potential energy of only 77 eV.

The coupled differential equations of the sputtering model are then as follows:

$$\frac{dC_{Ca}(\phi)}{d\phi} = \frac{1}{n_A}\left[-Y_{Ca}(\phi) + C_{Ca}^{b}\left(\sum_i Y_i(\phi)\right)\right]$$
$$\frac{dC_{Si}(\phi)}{d\phi} = \frac{1}{n_A}\left[-Y_{Si}(\phi) + C_{Si}^{b}\left(\sum_i Y_i(\phi)\right)\right]$$
$$\frac{dC_{O}(\phi)}{d\phi} = \frac{1}{n_A}\left[-Y_{O}(\phi) + C_{O}^{b}\left(\sum_i Y_i(\phi)\right)\right] \quad (1)$$

The surface concentration C_i of element i represents the relative concentration of the top monolayer, with n_A being the number of atoms per monolayer of 1.763×10^{15} at cm^{-2} for $CaSiO_3$. Its change over fluence ϕ is the result of two processes: (1) Each incoming ion sputters a mean number of Y_i atoms, which decreases the surface concentration of element i. (2) Any sputtered surface atom can be replaced by a bulk atom of element i with a probability that is equal the bulk concentration C_i^b (as an approximation, changes to the concentration of deeper layers are neglected here). This process increases C_i and is described by the second term in brackets. There the sum of sputtering yields with index i is taken over all target elements.

The kinetic sputtering yield Y_i^{kin} of element i is taken from the $CaSiO_3$ sputtering yield simulated with SDTrimSP $Y_i^{SDTrimSP}$ and rescaled with the fluence dependent concentration:

$$Y_i^{kin}(\phi) = Y_i^{SDTrimSP} \frac{C_i(\phi)}{C_i^b} \tag{2}$$

Therefore, the system of differential equations (1) is coupled via the sputtering yields as they are proportional to the respective element concentrations $C_i(\phi)$.

For Ca and Si only kinetic sputtering is calculated, while O sputtering is assumed to be the sum of a kinetic and a potential contribution:

$$Y_{Ca}(\phi) = Y_{Ca}^{kin}(\phi)$$

$$Y_{Si}(\phi) = Y_{Si}^{kin}(\phi)$$

$$Y_O(\phi) = Y_O^{kin}(\phi) + Y_O^{pot}(\phi)$$

(3)

For the potential sputtering yield, the following expression is used based on the observed linear dependence of sputtering yields on potential energy (see Figure 7):

$$Y_O^{pot}(\phi) = \gamma \frac{C_O(\phi)}{C_O^b}\left(E_{pot} - 2E_B\right) \tag{4}$$

The potential sputtering yield in O atoms/ion is here proportional to the surface O concentration C_O and the ion's potential energy E_{pot} minus twice the material's band gap E_B, which was kept as the potential sputtering threshold from Hijazi, et al. (2017) and Szabo, et al. (2018). The parameter γ describes how efficiently potential energy can cause desorption of O atoms and can be calculated from the measurement of the initial sputtering yields (see Figure 7). As mentioned in Section 3, for Ar and He different parameters γ had to be taken ($\gamma_{Ar} \approx 9.2$ [O atoms keV^{-1}] and $\gamma_{He} \approx 5.1$ [O atoms keV^{-1}]).

The total sputtering yield y in amu ion^{-1}, which is the quantity measured with a QCM setup, is calculated by summing up the products of elemental sputtering yields Y_i and atomic masses m_i:

$$y(\phi) = Y_{Ca}(\phi)m_{Ca} + Y_{Si}(\phi)m_{Si} + Y_O(\phi)m_O \tag{5}$$

The system of differential equations was solved numerically with Wolfram Mathematica 11.2 to calculate the fluence dependent surface concentrations. With these quantities the fluence dependent sputtering yields and steady state conditions can also be obtained. In the next sub-sections, the focus will be put on comparing steady state measurements with the corresponding sputtering yields $\lim_{\phi\to\infty} y(\phi)$.

4.2 Results for He Sputtering Yields

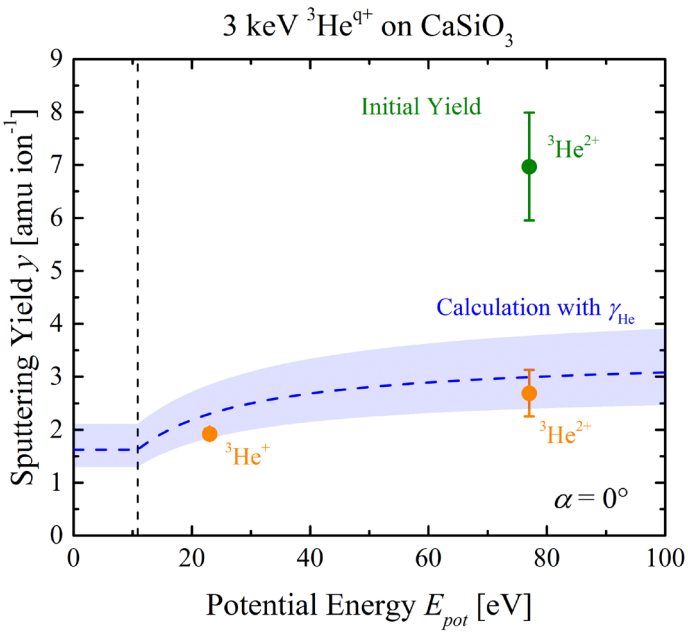

Figure 8: Comparison of the sputtering yields for ^{3}He sputtering plotted over the ion's potential energy. Measured steady state yields (orange) are compared to calculation results (blue dashed line) using the initial $^3He^{2+}$ yield (green).

Using the model introduced in Section 4.1, the steady state sputtering yields for He^{2+} can be well reproduced, as can be seen in Figure 8. There the blue dashed line shows the results when the parameter γ_{He} of the measured initial $^{3}He^{2+}$ sputtering yield is used. The shaded blue area represents an error estimate of the calculation based on errors of SDTrimSP simulations (~30% for He) and uncertainties in determining γ_{He}. For He^{2+}, potential sputtering plays an important role in preferentially sputtering O and due to the O depletion (see Figure 9 in Section 4.4) the sputtering yield decreases in good agreement with the experiment.

As mentioned before, our experiments do not indicate a universal potential sputtering scaling. This behavior does not agree with the findings by Hijazi, et al. (2017) or our previous assumptions. Varying values for γ_{Ar} and γ_{He} could be explained by the phenomenon of kinetically assisted potential sputtering, which was observed previously for MgO_x samples (Hayderer, et al. 2001b). Here potential sputtering was found to be proportional to the kinetic energy of the impacting ion (in addition to the potential energy), which would be in accordance with the different He and Ar energies.

Otherwise, the calculation for the steady state yields using the Ar potential sputtering behavior as a universal scaling γ_{Ar} also shows a reasonable agreement. Steady state sputtering yields are only 5% higher than for the γ_{He} calculation and therefore also reproduce He^{2+} measurements. The potential energy of He^{+} (24 eV) might be high enough to cause changes in the sample surface's elemental composition. He^{2+} yields have always been recorded after sufficient He^{+} bombardment to avoid complications due to He implantation (see Section 3.1). But if He^{+} already causes preferential O depletion, this could explain lower measured He^{2+} initial yields (i.e. an underestimation of the efficiency parameter γ). However, differences between γ_{Ar} calculation and the measured He^{+} yield are quite significant and agree much better when γ_{He} is used.

Analysis of our calculations shows that different surface binding energy models and possible variations in the sample composition noticeably affect the outcome. Due to these uncertainties, no definitive recommendation can be given about which of the two γ parameters should be used because the steady state behavior of He^{2+} can be described well in both cases. Nevertheless, total agreement for γ_{He} is better, which is why the He calculations in the following sections show results based on γ_{He} potential sputtering.

4.3 Results for Ar Sputtering Yields

The calculation is also able to reproduce very well how the initial linear dependence of the potential sputtering yield with E_{pot} develops into a much less pronounced dependence for the steady state yield on the ion's potential energy as shown in Figure 7. As a comparison with the experimental yields, the calculated steady state yields are included in Figure 7 as the dashed blue line. The shaded area again gives an uncertainty estimate for this calculation. Even though a simple model was used, the absolute values of the calculated steady state yields agree very well with all measured Ar charge states.

4.4 Steady State Oxygen Concentrations

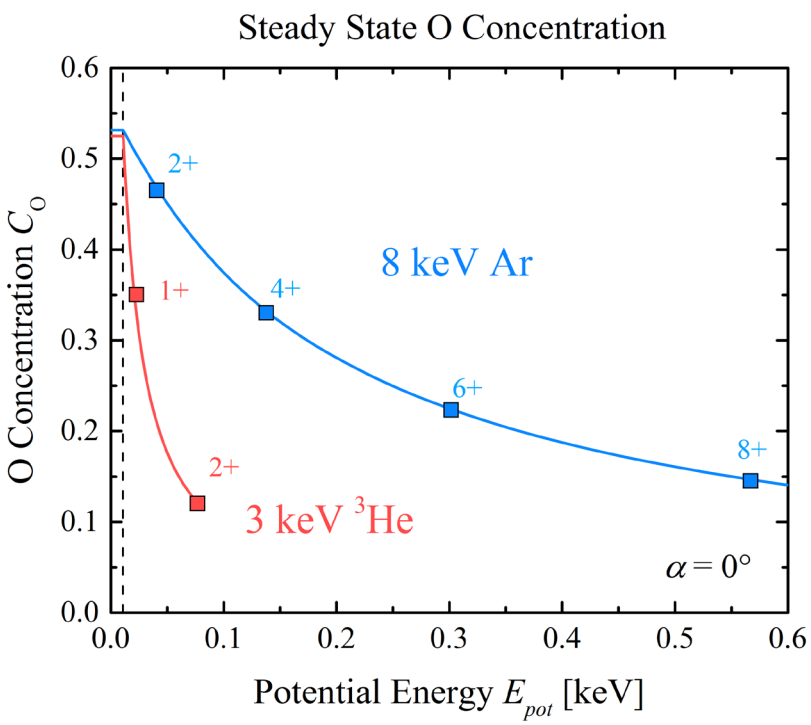

Figure 9: Calculated steady state O concentrations for normal incidence irradiation are plotted over the ion's potential energy. For Ar (blue), O depletion is not as severe as for He (red) because more Ca and Si is **removed** by kinetic sputtering. For He (red), potential sputtering is dominant already at lower potential energy and O depletion is much more significant.

With our model we have successfully linked different effects of potential sputtering in cases of He and Ar bombardment to the depletion of surface O. The steady state O concentration is shown in Figure 9 for He (red, using γ_{He}) and Ar (blue) charge states. For He, potential sputtering is dominant at the beginning of the irradiation causing a strong depletion of surface O (see the sputtering yield measurement shown in Figure 5). As the potential sputtering is assumed to be proportional to the O concentration, its contribution is smaller than expected in the steady state when compared to kinetic sputtering alone (see the comparison between steady state yield and SDTrimSP simulations in Figure 5). In contrast, for Ar irradiation kinetic sputtering plays an important role in exposing fresh bulk O atoms at the surface. Ca and Si are sputtered more efficiently than by He ion impact, which leads to a higher O concentration in the steady state compared to He with the same potential energy. Therefore, higher differences can be observed between experimental steady state yields including potential sputtering and the kinetic sputtering yield alone (see Figure 6).

Consequently, kinetic and potential sputtering in the steady state cannot be treated independently, but their interplay is important to understand the development of the sputtering yield.

4.5 Implications for Planetary Surfaces Exposed to the Solar Wind

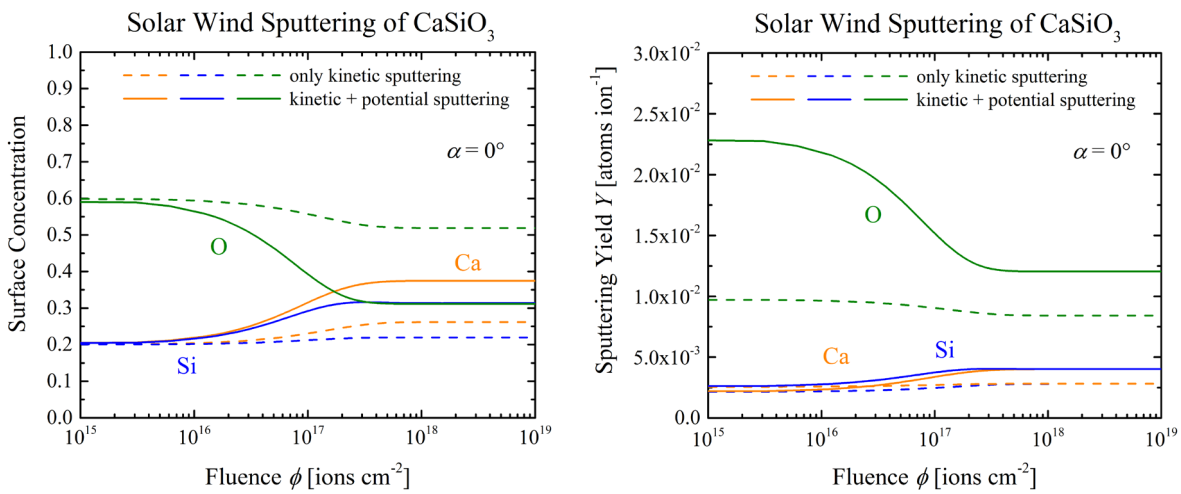

Figure 10: Left: Fluence dependence of the calculated surface concentration changes resulting from solar wind sputtering of $CaSiO_3$, assuming a solar wind

composition of 96% H^+ and 4% He^{2+}. Dashed lines represent the concentrations for Ca (orange), Si (blue) and O (green) with kinetic sputtering only. Full lines include both kinetic sputtering of H and He as well as potential sputtering by He^{2+} ions. Right: Depiction of the fluence dependence of the respective sputtering yields under 96% H^+, 4% He^{2+} solar wind bombardment. In the steady state case potential sputtering increases all yields by about 40%.

	H	**H, He (KS)**	**H, He (KS and PS)**
$\mathbf{C_{Ca}}$	0.263	0.262 (-0.4%)	0.374 (+42%)
$\mathbf{C_{Si}}$	0.219	0.219 (±0.0%)	0.314 (+43%)
$\mathbf{C_{O}}$	0.518	0.519 (+0.2%)	0.312 (-40%)
$\mathbf{Y_{Ca}}$	2.34×10^{-3}	2.81×10^{-3} (+20%)	4.01×10^{-3} (+71%)
$\mathbf{Y_{Si}}$	2.34×10^{-3}	2.81×10^{-3} (+20%)	4.01×10^{-3} (+71%)
$\mathbf{Y_{O}}$	7.02×10^{-3}	8.42×10^{-3} (+20%)	1.20×10^{-2} (+71%)

Table 1: Calculated steady state concentrations C_i and sputtering yields Y_i for each element. Three scenarios were modeled: only proton sputtering ("H"), H and He with kinetic sputtering ("H, He (KS)") and H and He with kinetic and potential sputtering ("H, He (KS and PS)"). Relative atomic concentrations are shown and the sputtering yields are given in atoms ion^{-1}. Numbers in brackets give the relative difference to the results of only proton sputtering.

The interplay of kinetic and potential sputtering is also very important for the solar wind in general, where mainly H^+ and He^{2+} bombard mineral surfaces of atmosphere-less bodies at the same time. Figure 10 shows the results from a simulation of these effects by modelling solar wind sputtering with 96% H^+ and 4% He^{2+} (Russell, Luhmann, & Strangeway 2016) under normal incidence.

Kinetic sputtering yields are taken from SDTrimSP simulations with adapted input parameters as described in the Appendix. For H sputtering, these simulations predict 0.26 amu ion^{-1} in good agreement with previously published values (Szabo, et al. 2018). The changes of the surface concentrations for Ca (orange), Si (blue) and O (green) as a result of ion sputtering are plotted over ion fluence on the left image, while the right image shows the development of the respective yields. Two calculations are compared: dashed lines represent modelling of only kinetic sputtering effects, while full lines include potential sputtering by He^{2+} ions.

Furthermore, the effect of only proton sputtering was calculated, but is not shown in Figure 10. The results for all three scenarios are listed in Table 1.

With potential sputtering, a clear O depletion by 48% to a surface concentration of 0.31 is predicted as a result of potential sputtering. Compared to only proton sputtering, the steady state O content is smaller by 40% when potential sputtering is included, similar to the 22% calculated for KREEP lunar analogue material (Barghouty, et al. 2011), 27% for anorthite (Hijazi, et al. 2017) and 26% for JSC-1A lunar regolith simulant (Alnussirat, et al. 2018). This is caused solely by the potential sputtering as the concentrations are barely affected by just including kinetic sputtering by He ions. This has also resulted from the calculations for other analogue materials (Alnussirat, et al. 2018; Barghouty, et al. 2011; Hijazi, et al. 2017).

On the other hand, all sputtering yields are increased by including the potential sputtering effects. O atoms are sputtered by the potential energy, while Ca and Si erosion is increased because of the change in surface concentration. In the steady state, where the ratio between yields represents the bulk ratio, all sputtering yields are increased by 43% compared to kinetic sputtering only (full versus dashed lines in Figure 10). The yield increase compared to proton sputtering is 71%, which is in the same order as 52% on KREEP (Barghouty, et al. 2011) and 46% on anorthite (Hijazi, et al. 2017). Just including He kinetic sputtering causes a total sputtering yield increase of only 20% (similar to the 26% reported for KREEP (Barghouty, et al. 2011) and 25% anorthite (Hijazi, et al. 2017)).

Our results therefore underline the importance of including at least He^{2+} to solar wind modelling in accordance to previously published work. Further minor effects are then to be expected for multiply charged heavy ions. Changes in surface composition as well as increases in sputtering yield both give a consistent picture based on a model that can reproduce experimental sputtering yields.

5. SUMMARY AND CONCLUSION

Sputtering yields of $CaSiO_3$ were measured under irradiation with singly and doubly charged He ions at solar wind velocity. For He^+ the two isotopes $^3He^+$

and $^{4}He^{+}$ show identical sputtering yields when measured at equal impact velocity. Therefore, data obtained for sputtering with 3 keV ^{3}He can represent the ^{4}He contribution of the solar wind, because both kinetic sputtering and potential energies are equal. Measured sputtering yields agree very well with SDTrimSP simulations with adapted parameters. For He^{2+}, high initial potential sputtering yields could be observed, which are followed by an exponential decrease until a steady state is reached after the removal of a few monolayers of material. This behavior is consistent with new, more detailed 8 keV Ar^{8+} measurements and indicates a strong depletion of surface O due to potential sputtering. Using in-situ re-prepared surfaces, Ar sputtering yields at the beginning of the irradiation were found to have a linear dependence on the ion's potential energy. However, initial potential sputtering yields for 8 keV Ar and 3 keV $^{3}He^{2+}$ were found to have a different potential energy scaling.

A model with a set of coupled differential equations was applied to calculate the prolonged effects of He and Ar sputtering, assuming a potential sputtering yield that is linearly dependent on the surface O concentration and the ion's potential energy. This model is able to explain how the observed (initial) linear dependence on potential energy turns into much less pronounced changes for higher potential energies in the steady state case. Absolute values for the steady state sputtering yields can be reproduced very well for both He and Ar ions. The calculation therefore indicates that the assumption of only O atoms being potentially sputtered is reasonable and potential sputtering of $CaSiO_3$ proceeds according to the defect-mediated sputtering model. The development of the sputtering yield during the irradiation is dominated by the interplay of kinetic and potential sputtering, leading to significant differences in He and Ar sputter yields. Kinetic sputtering plays an important role to increase the surface O concentration in the steady state, which in turn causes a rise in potential sputtering.

Based on our findings, the effects of solar wind sputtering with H^{+} and He^{2+} on $CaSiO_3$ were estimated. Both a significant O depletion as well as an increase in all elemental sputtering is predicted, mainly due to the potential sputtering component of the solar wind He^{2+}. These results agree well with previous calculations for other materials.

Our experimental findings have been consistently verified by modelling O desorption as a result of potential sputtering, based on the defect-mediated model of potential sputtering and previous experimental findings. Nevertheless, future experiments should aim to verify the predicted O

depletions with in-situ sample analysis. In space, O reduction has been observed on the Moon, where the darkening and reddening of the lunar surface has been connected to the formation of nanophase Fe particles assumed to originate via disassociation from regolith minerals (Kohout et al. 2014; Pieters & Noble 2016). Even though micrometeorite impacts are expected to significantly contribute to the formation of such nanoparticles (Sasaki et al. 2001), these observations support that O depletion by potential sputtering plays a role during space weathering. Furthermore, experiments should continue with more samples to investigate how much potential sputtering can vary for different minerals. Due to the interplay between kinetic and potential sputtering, also the effect on other interesting species such as Na for Mercury should be quantified.

Another aspect that should be taken into account for future experiments is how different temperatures affect potential sputtering. As can be seen in Figure 10, steady state for H+He sputtering is reached after a fluence of about 10^{18} ions cm^{-2}, which corresponds to a few 100 years of exposure for a solar wind flux at the Moon of about 10^{8} ions cm^{-2} s^{-1} (Russell, et al. 2016). This is a short time on an astronomical scale, but for elevated surface temperatures diffusion will affect the surface concentrations. This could affect space weathering on the Moon (up to 400 K), but should especially be a concern for Mercury's expected maximum temperatures of 700 K (Vasavada, Paige, & Wood 1999). It has to be investigated whether this will bring more O to the surface, which would lead to an even more pronounced role of potential sputtering.

Solar wind sputtering research would also greatly benefit from improvements in simulations. The presented model predicts experimental steady state sputtering yields very well, but some limitations have become apparent. For example, the model overestimates the fluence needed until steady state is reached for both He (by a factor of 2) and Ar (by a factor of 5). In the case of Ar irradiation, several keV of kinetic energy are deposited within a few nanometers underneath the surface. Surface O depletion would therefore be affected by intermixing of atomic layers in the collision cascade. This is an effect that goes beyond the presented calculations. Including some potential sputtering effects in already established BCA codes, similar as it is done for chemical sputtering of C in SDTrimSP (Mutzke, et al. 2019), would therefore significantly enhance simulations of cases relevant for solar wind sputtering.

ACKNOWLEDGEMENTS

Financial support has been provided by the Austrian Science Fund FWF (Project No. I 4101-N36) and by KKKÖ (Commission for the Coordination of Fusion research in Austria at the Austrian Academy of Sciences - ÖAW) as well as the Swiss National Science Foundation Fund (200021L_182771/1). Support by VR-RFI (contracts #821-2012-5144, #2017-00646_9 & 2018-04834) and the Swedish Foundation for Strategic Research (SSF, contract RIF14-0053) supporting operation of the accelerator at Uppsala University is gratefully acknowledged.

The computational results presented have been achieved using the Vienna Scientific Cluster (VSC). The authors are grateful to Michael Schmid (IAP, TU Wien) for his continued support with the QCM electronics.

APPENDIX

SDTrimSP Simulations

From the QCM measurements, only the total sputtering yields in amu/ion can be determined, but there is no direct information available about how sputtering distributes among Ca, Si and O. The goal is to find a set of simulation parameters that consistently describes the measured total sputtering yields.

As was already reported in earlier investigations (Szabo, et al. 2018), default parameters for SDTrimSP simulations overestimate measured sputtering yields. The atomic density ρ and surface binding energies were adapted to improve the agreement between experimental findings and SDTrimSP simulations.

As a default method in SDTrimSP, the atomic density of compound samples is calculated from tabulated values for the different elements. In the case of $CaSiO_3$, the calculated density from the individual elemental densities give a value of 0.0376 at $Å^{-3}$, which is significantly lower than the $CaSiO_3$ bulk density of 0.07412 at $Å^{-3}$ (corresponding to 2.86 g cm^{-3}). For the case of solid-gas compounds, an adaption of the density of the gaseous component is recommended (Möller & Posselt 2001). The $CaSiO_3$ bulk density of 2.86 g cm^{-3} is realized by setting the bounded O elemental density to 0.7 at $Å^{-3}$ using the parameter dns_0 in the input file "tri.inp". This density was used in all our simulations.

However, a valid choice of surface binding energies is more important for the simulations. Different elemental surface binding energies will affect the sputtering yields of each element. This will play a role especially for the potential sputtering calculations presented in Section 4, where different kinetic O sputtering yields affect the outcome.

One key observation is made in Section 3.3: After a potential sputtering experiment, preparing sample surfaces by oxygen flooding or by cleaning with 2 keV Ar^+ sputtering leads to accordant Ar^{q+} initial sputtering yields within their experimental error bars. The sample can therefore be expected to have a similar composition after both preparation methods. During potential sputtering, O depletion occurs and therefore O flooding replenishes the surface O content. We suspect the same effect from Ar^+

sputtering as we measure the same sputtering yields. Therefore, it can be assumed that the surface composition after both methods is similar and that Ar^+ sputtering does not cause a significant O depletion. The ratio of Ca, Si and O sputtering yields should therefore be comparable to the $CaSiO_3$ composition ratio of 1:1:3.

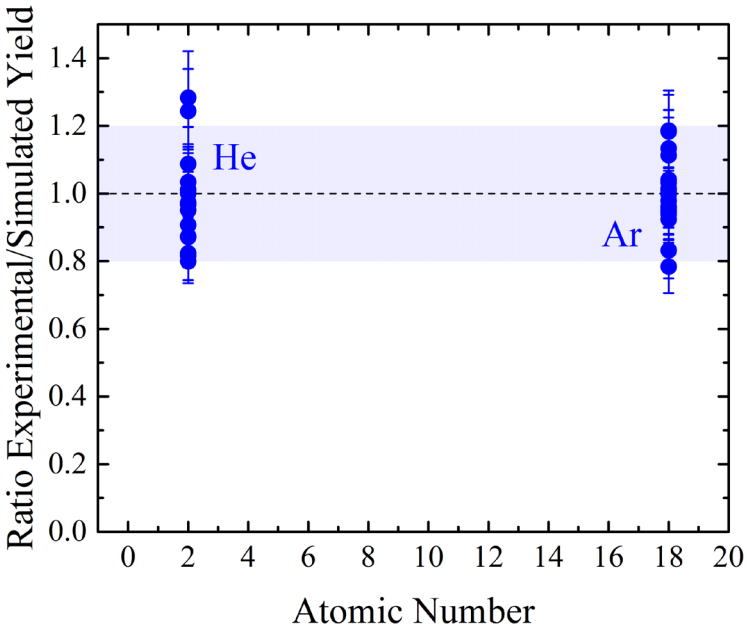

Figure 11: Compilation of the ratio between experimental and simulated sputtering yields using the $CaSiO_3$ bulk density and an adapted surface binding energy. Measured data includes different kinetic energy for ^3He (3 keV), ^4He (1 keV, 2 keV, 4, keV) and Ar (1 keV, 2 keV, 4 keV). Most ratios lie within the blue shaded area of 0.8 – 1.2.

With an increased O surface binding energy of 6.5 eV (instead of the tabulated value of 2.58 eV, which is half the oxygen dissociation enthalpy ΔH^{diss} = 5.15 eV) and with the simulation parameter "isbv=2" we found a good agreement between the simulation results and the experimental observations. As Figure 3 in Section 2.3 shows, the angular dependence of 2 keV Ar^+ sputtering is very precisely reproduced (blue curve) compared to default densities and surface binding energies (green). The ratios of sputtering yields is on average $Y_{Ca}:Y_{Si}:Y_O$ = 0.76 : 0.86 : 3, which is near the expected ratio of 1:1:3.

A good agreement for the total yield is also found for Ar, ^3He and ^4He at energies between 1 and 4 keV, as it can be seen in Figure 11. There the ratio between experimental and simulated yield is plotted, which mostly

lies between 0.8 and 1.2 (blue shaded area). Its average value of 0.99 indicates that no systematic offset exists.

Dynamic SDTrimSP simulations performed with these adapted parameters show a close to constant total sputtering yield in amu/ion. This agrees with our experiments with fluences in the range of multiple 10^{15} ions cm^{-2}.

Closer experimental in-situ investigations of surface concentration changes should be aimed for in the future. Consequently, a better adaptation of the simulation parameters could be performed that relies on observations of the sputtering yield as well as surface concentration changes.

However, with our adapted parameters we have found a description of $CaSiO_3$ kinetic sputtering that is in consistently good agreement with our experimental results.

REFERENCES

Alnussirat, S. T., Barghouty, A. F., Edmunson, J. E., Sabra, M. S., & Rickman, D. L. 2018, Nuclear Instruments and Methods in Physics Research Section B: Beam Interactions with Materials and Atoms, 420, 33

Arredondo, R., et al. 2019, Nuclear Materials and Energy, 18, 72

Aumayr, F., & Winter, H. 2004, Philosophical Transactions of the Royal Society of London A: Mathematical, Physical and Engineering Sciences, 362, 77

Barghouty, A. F., Meyer, F. W., Harris, P. R., & Adams, J. H. 2011, Nuclear Instruments and Methods in Physics Research Section B: Beam Interactions with Materials and Atoms, 269, 1310

Behrisch, R., & Eckstein, W. 2007, Sputtering by Particle Bombardment: Experiments and Computer Calculations from Threshold to MeV Energies (Springer Science & Business Media)

Cremonese, G., Bruno, M., Mangano, V., Marchi, S., & Milillo, A. 2005, Icarus, 177, 122

Deer, W. A., Howie, R. A., & Zussman, J. 1997, Rock-forming minerals: single-chain silicates, Volume 2A

DREEBIT. 2018, DREEBIT - Ionization Energy Database

Hapke, B. 2001, Journal of Geophysical Research: Planets, 106, 10039

Hayderer, G., et al. 2001a, Nuclear Instruments and Methods in Physics Research Section B: Beam Interactions with Materials and Atoms, 182, 143

Hayderer, G., et al. 2001b, Physical Review Letters, 86, 3530

Hayderer, G., Schmid, M., Varga, P., Winter, H. P., & Aumayr, F. 1999a, Review of Scientific Instruments, 70, 3696

Hayderer, G., et al. 1999b, Physical Review Letters, 83, 3948

Hijazi, H., Bannister, M., Meyer, H., Rouleau, C. M., & Meyer, F. 2017, Journal of Geophysical Research: Planets, 122, 1597

Hijazi, H., Bannister, M. E., Meyer, H. M., Rouleau, C. M., Barghouty, A. F., Rickman, D. L., & Meyer, F. W. 2014, Journal of Geophysical Research: Space Physics, 119, 8006

Kallio, E., & Janhunen, P. 2003, Geophysical Research Letters, 30

Kelly, R. 1980, Surface Science, 100, 85

Killen, R., et al. 2007, Space Science Reviews, 132, 433

Kohout, T., et al. 2014, Icarus, 237, 75

Malherbe, J., Hofmann, S., & Sanz, J. 1986, Applied Surface Science, 27, 355

Meyer, F. W., Harris, P. R., Taylor, C. N., Meyer III, H. M., Barghouty, A. F., & Adams, J. H. 2011, Nuclear Instruments and Methods in Physics Research Section B: Beam Interactions with Materials and Atoms, 269, 1316

Möller, W. 2014, Nuclear Instruments and Methods in Physics Research Section B: Beam Interactions with Materials and Atoms, 322, 23

Möller, W., & Posselt, M. 2001, in TRIDYN User Manual

Mutzke, A., Schneider, R., Eckstein, W., Dohmen, R., Schmid, K., Toussaint, U. v., & Badelow, G. 2019, in IPP-Report

Neidhart, T., Pichler, F., Aumayr, F., Winter, H., Schmid, M., & Varga, P. 1995a, Physical Review Letters, 74, 5280

Neidhart, T., Pichler, F., Aumayr, F., Winter, H., Schmid, M., & Varga, P. 1995b, Nuclear Instruments and Methods in Physics Research Section B: Beam Interactions with Materials and Atoms, 98, 465

Oberkofler, M., et al. 2015, Fusion Engineering and Design, 98, 1371

Pfleger, M., et al. 2015, Planetary and Space Science, 115, 90

Pieters, C. M., & Noble, S. K. 2016, Journal of Geophysical Research: Planets, 121, 1865

Russell, C. T., Luhmann, J. G., & Strangeway, R. J. 2016, Space Physics: An Introduction (Cambridge University Press)

Sasaki, S., Nakamura, K., Hamabe, Y., Kurahashi, E., & Hiroi, T. 2001, Nature, 410, 555

Schenkel, T., Barnes, A., Hamza, A., & Schneider, D. 1998, The European Physical Journal D-Atomic, Molecular, Optical and Plasma Physics, 1, 297

Sigmund, P. 1969, Physical Review, 184, 383

Sporn, M., et al. 1997, Physical Review Letters, 79, 945

Stadlmayr, R., et al. 2018, Nuclear Instruments and Methods in Physics Research Section B: Beam Interactions with Materials and Atoms

Stadlmayr, R., Szabo, P. S., Mayer, D., Cupak, C., Möller, W., & Aumayr, F. 2019, Physica Scripta

Szabo, P. S., et al. 2018, Icarus, 314, 98

Varga, P., Neidhart, T., Sporn, M., Libiseller, G., Schmid, M., Aumayr, F., & Winter, H. 1997, Physica Scripta, 1997, 307

Vasavada, A. R., Paige, D. A., & Wood, S. E. 1999, Icarus, 141, 179

Wirtz, L., et al. 2000, Surface science, 451, 197

Wurz, P. 2005. in The Dynamic Sun: Challenges for Theory and Observations, Solarwind composition (Nordwijk, The Netherlands: ESA SP-600), 1

Wurz, P., Gamborino, D., Vorburger, A., & Raines, J. 2018, Journal of Geophysical Research: Space Physics, 124, 2603

Wurz, P., Rohner, U., Whitby, J. A., Kolb, C., Lammer, H., Dobnikar, P., & Martín-Fernández, J. A. 2007, Icarus, 191, 486

Yamashita, N., et al. 2012, Earth and Planetary Science Letters, 353, 93

Ziegler, J. F., Ziegler, M. D., & Biersack, J. P. 2010, Nuclear Instruments and Methods in Physics Research Section B: Beam Interactions with Materials and Atoms, 268, 1818